SPECIAL ISSUE ARTICLE



Check for updates

Mechanical characterization of boron carbide single crystals

Arezoo Zare^{1,2} | Mo-Rigen He^{1,2} | Michael Straker³ | M. V. S. Chandrashekhare⁴ | Michael Spencer^{5,6} | Kevin J. Hemker^{1,2} | James W. McCauley^{1,2} | K. T. Ramesh^{1,2}

¹Department of Mechanical Engineering, The Johns Hopkins University, Baltimore, Maryland, USA ²Hopkins Extreme Materials Institute, The Johns Hopkins University, Baltimore, Maryland, USA ³Department of Physics and Engineering Physics, Morgan State University, Baltimore, Maryland, USA ⁴Department of Electrical Engineering, University of South Carolina, Columbia, South Carolina, USA ⁵Department of Electrical and Computer Engineering, Morgan State University, Baltimore, Maryland, USA ⁶Department of Electrical and Computer Engineering (Emeritus), Cornell University, Ithaca, New York, USA

Correspondence

Arezoo Zare, Department of Mechanical Engineering, The Johns Hopkins University, Baltimore, MD 21218, USA. Email: azare1@jhu.edu

Funding information

Army Research Laboratory, Grant/Award Number: W911NF-12-2-0022

Abstract

Out-of-plane anisotropy in the mechanical response of boron carbide was studied by performing nanoindentation experiments on four specific crystallographic orientations of single crystals, that is, $(\overline{2}1116)$, $(\overline{3}212)$, $(\overline{3}\overline{3}64)$, and $(14\overline{5}7)$. For each orientation of the single crystals, in-plane variations of indentation modulus and hardness were also studied by monitoring the relative rotation between the crystal surface and a Berkovich indenter tip. A significant out-of-plane anisotropy in indentation modulus was observed with ~80 GPa difference between the highest and lowest values. A smaller but measurable out-of-plane anisotropy in indentation hardness was also observed. In-plane anisotropy, on the other hand, was found to be significantly influenced by the scatter in the data and geometrical imperfections of the indenter tip. Investigations of indentation pop-in events suggested that deformation is entirely elastic prior to the first pop-in. Furthermore, quasi-plastic flow along the (21116) orientation of the single crystals was found to be more homogeneous than the other tested orientations. For select indents, cross-sectional transmission electron microscopy (TEM) of the indented regions showed formation of a quasi-plastic zone in the form of lattice rotation and various microstructural defects. The quasi-plastic zone grew in size with increasing the indentation depth. The TEM observations also suggested the crystal slip to be a potential mechanism of quasi-plasticity and a precursor for formation of amorphous bands that could eventually lead to cracking and fragmentation. The proposed failure mechanism provides valuable insights for calibrating constitutive computational models of failure in boron carbide.

KEYWORDS

boron carbide, deformation, nanoindentation, single crystals

1 | INTRODUCTION

Boron carbide has a nominal stoichiometry of B_4C and is comprised of 12-atom boron-rich icosahedra (located at the vertices of a rhombohedral unit cell of trigonal symmetry) that are connected by three-atom chains of

carbon and/or boron along the [111] rhombohedral axis. Alternatively, the crystal structure can be described by a non-primitive hexagonal unit cell with the [0001] hexagonal axis coinciding with the [111] rhombohedral direction. The extended network of icosahedral units and strong covalent bonds give boron carbide a low density

(2.52 g/cm³), high hardness (Vickers hardness of ~30 GPa), high melting temperature (2450°C), and high thermal and chemical stability. These properties make boron carbide desirable for mechanical, electronic, refractory, and nuclear applications.^{1,2}

Our particular interest is in the potential use of boron carbide as a protective material against impact conditions, where it performs well for lower-velocity impact. However, boron carbide appears to lose strength when impacted at high velocities, and several studies have suggested that this is a consequence of the mechanism of amorphization.³ Although mechanical response of boron carbide has been extensively studied over the last two decades, 2,4-9 there is still no consensus on the mechanisms that result in amorphization (e.g., carbon cluster formation vs. three-atom chain bending and icosahedra breaking^{6,7,9}). A clear understanding of this mechanism is essential for designing boron carbide ceramics with improved mechanical performance under impact conditions. Using single crystals for characterization of mechanical response could reduce uncertainties resulted from the commonly observed variations in free carbon content among different grains in polycrystalline specimens. ¹⁰ Furthermore, single crystals with known orientations could help clarify the effects of crystal anisotropy on the mechanical response.¹¹ This is of particular importance because boron carbide has been reported to have highly anisotropic mechanical properties. Resonant ultrasound spectroscopy measurements of B_{5.6}C single crystals suggested significant anisotropy in elasticity, with global values of "Young's modulus" that vary by a factor of 8 along different crystallographic orientations.12 These measurements also showed that while Young's modulus is orientation-independent on the (0001) plane, it is strongly orientation-dependent on the $(\overline{1}012)$, $(10\overline{1}0)$, and $(1\overline{2}12)$ planes. 12 The anisotropic elasticity of the single crystal is important in part because one model for the onset of amorphization is based on the concept of the Born instability, which is computed from the elastic modulus tensor. 13 We note here that the anisotropic modulus tensor is dependent on the stoichiometry and is also a function of the applied hydrostatic pressure, 13,14 so that the amorphization threshold would also depend on stoichiometry and pressure. Investigations of anisotropy in the hardness of boron carbide single crystals have been limited. Nanoindentation experiments on B_{4,3}C single crystals¹⁰ showed only 1 GPa difference between the indentation hardness of the $(0\ 0\ 1)$ and $(1\ 0\ \overline{1}\ 1)$ planes. However, in-plane variations of indentation hardness were not considered in this study.¹⁰

In the present study, we use the optical floating zone technique to grow boron carbide crystal boules with large single crystal regions, and then study their mechanical response and deformation mechanisms using a combination

of quasi-static nanoindentation and electron microscopy. Despite different strain rates and boundary conditions between quasi-static and impact conditions, mechanical properties obtained from quasi-static experiments can be used as a measure of gross impact performance. For example, elastic modulus and hardness are both positively correlated to ballistic performance. 15-18 This can be rationalized because materials with higher stiffness can better resist the large flexural deflections induced by projectile impact. 15,17 Higher hardness could also contribute to increased penetration resistance by plastically deforming, fracturing, and deflecting the projectile. 15,17 Quasi-plastic deformation is also believed to be an important factor affecting the impact performance of ceramics. 16,18 Unlike conventional tensile or compression testing, during nanoindentation the hydrostatic constraint imposed by the indenter delays fracture and catastrophic failure, thereby allowing for investigations of both the elastic and quasi-plastic responses of the crystals.

2 | EXPERIMENTAL METHODS

2.1 | Preparation of single crystals

Boron carbide crystals were grown via the floating zone technique 10-12,19,20 in a furnace that utilizes xenon lamps as a heat source. Crystal boules with a diameter of ~8 mm were grown from polycrystalline starting rods that were 10 mm in diameter and 10 cm in length. The starting rods were hot-pressed from 99.9% pure B₄C powder by a commercial vendor (Testbourne Ltd.). Inside the furnace, the starting rods were heated from 0% to 70% lamp power over 2.5 h and continuously rotated in opposite directions at 10 rpm to facilitate mixing. The growth process was monitored by a camera in real time. In the rendered images, molten zones of the starting rods showed a distinct texture/color from the adjacent solid materials. At a lamp power of ~65%, a distinct solid-liquid interface was established, and the molten zone was seen to retain its shape and size without any signs of instability. At this stable growing condition, the growth rate of the crystal boules was 10 mm/h. To mitigate oxidation, an argon gas flow of 0.3–1.5 L/min was used inside the furnace. X-ray energy dispersive spectrometry (XEDS) measurements on smaller diameter (4 mm) crystal boules identified their stoichiometry as B_{4 9}C. Details of these measurements are reported in our earlier study.¹¹

Our previous studies showed that under the aforementioned growth conditions, the crystal boules tend to grow close to the [0001] direction. Whitebeam X-ray Laue diffraction with a spot size of 1 mm was used to align the crystal boules prior to sectioning. The obtained

diffraction patterns were compared to simulated patterns of the rhombohedral crystal structure to confirm the orientation. The Laue diffraction patterns of the (0001) and (10 $\overline{1}0$) planes were found to be, respectively, 15–20° and 45–50° away from the growth direction. Once the desired orientations were identified, a low-speed diamond saw was used to section 7–8 mm thick slices which were subsequently polished to a mirror-finish surface using diamond lapping films.

The growth quality of the sectioned and polished slices was evaluated using electron backscatter diffraction (EBSD) in a Helios G4 UC DualBeam system (ThermoScientific) operating in the scanning electron microscope (SEM) mode. An accelerating voltage of 20 kV and a probe current of 13 nA were used. Twin-free single crystal regions were identified and marked.

2.2 | Characterization of mechanical response and deformation mechanisms

An iNano nanoindenter with an InForce50 actuator (Nanomechanics Inc., now KLA corporation) was used to measure the anisotropy in indentation modulus and hardness. All indentations were performed within the twin-free single crystal regions identified by EBSD characterization. To characterize both elastic and quasi-plastic deformation in boron carbide (and similarly hard materials), a sharp indenter tip must be used. Among the commonly used sharp tips, square-based pyramids (Knoop and Vickers) are prone to "chisel edge" where the four faces do not meet at a single point, thereby resulting in ill-defined area function and asymmetric impressions. Triangular-based pyramids (Berkovich and cube corner), on the other hand, offer a small rounding at the apex of the indenter (~20 nm radius when brand new) and thus facilitate the attainment of quasi-plasticity at lower applied loads. Although cube corner tips (with a centerline-to-face angle of 35.26°) are sharper than Berkovich (with an angle of 65.27°), they are not preferred for the measurements of indentation modulus and hardness due to the possibility of formation of large radial cracks in brittle materials.²¹ Therefore, all indentations in the present study were performed using a diamond Berkovich indenter, which was assumed to be elastically isotropic. In-plane variations of indentation modulus and hardness were also studied by monitoring the relative orientation between the crystal surface and the Berkovich indenter.

To obtain properties as a function of indentation depth, the continuous stiffness measurement (CSM) technique was employed. In this technique, contact stiffness (S) is measured continuously during the loading of the indenter by superimposing an oscillatory load, with an amplitude

of P_0 and a frequency of ω , on the load signal and measuring the amplitude (h_0) and phase (ϕ) of the corresponding displacement signal by means of a frequency-specific amplifier^{22–24} using:

$$\frac{1}{S} = \frac{1}{\left(\frac{P_0}{h_0}\right)\cos\varnothing - \left(K_i - m\omega^2\right)} - \frac{1}{K_f},\tag{1}$$

where K_i is the stiffness of the indenter column, K_f is the stiffness of the instrument's frame, and m is the mass of the indenter. The obtained stiffness is then used to calculate indentation modulus ($E_{\rm IT}$) and hardness ($H_{\rm IT}$) using the original Oliver and Pharr method²⁵:

$$E_{\rm IT} = \frac{1 - (\nu_{\rm s})^2}{\frac{1}{E_{\rm r}} - \frac{1 - (\nu_{\rm i})^2}{E_{\rm i}}},$$
 (2)

$$H_{\rm IT} = \frac{F_{\rm max}}{A_{\rm P}},\tag{3}$$

where $v_{\rm s}$ is the Poisson's ratio of the specimen (0.17¹), $v_{\rm i}$ is the Poisson's ratio of the indenter (0.07), $E_{\rm i}$ is the Young's modulus of the indenter (1141 GPa), and $E_{\rm r}$ is the reduced elastic modulus ($E_{\rm r} = (S/2) \left(\pi/A_{\rm p}\right)^{\wedge}$ 0.5) with $A_{\rm p}$ and $F_{\rm max}$ being the projected contact area and maximum applied load, respectively. The projected contact area was determined through knowledge of the indenter's area function and the depth over which the indenter and specimen are in contact. The area function of the indenter was calibrated by performing indentations in a fused silica reference specimen. The CSM indentations were performed under an applied indentation strain rate (time derivative of the load divided by the load at each point in time) of 0.1 s⁻¹ to a maximum indentation depth of ~300 nm.

To study the indentation pop-in phenomenon, additional nanoindentation experiments were performed without the superimposed CSM oscillations. The loading sequence for these indentations consisted of loading at 0.33 mN/s to a maximum load of 10 mN, a 1(one) s hold at the maximum load, unloading to 10% of the maximum load at a constant rate equal to the loading rate, an 80 s hold at 10% of maximum load to measure and correct for thermal drift, and final unloading. The residual impressions of select indentations were characterized with a Tescan Mira field emission SEM using an accelerating voltage of 4 kV.

To study indentation cracking, a nanoindenter XP (MTS, Agilent Technologies) was used to perform indentations on select single crystal regions to a maximum indentation depth of \sim 1 μ m. Evaluation of indentation modulus

and hardness was not attempted from these indentations because of the formation of the large cracks.

To understand the underlying deformation mechanisms, for select indentations focused-ion beam (FIB) machining was used to lift out cross-sectional specimens under the indentations, and the extracted specimens were polished to electron-transparency using 30 kV Ga⁺ ions (beam current 2–21 nA). The cross-sections were then cleaned using 5 kV Ga⁺ ions (beam current ~40 pA) and studied by transmission electron microscopy (TEM) using a TF30 S/TEM (ThermoScientific) instrument operating at 300 kV.

3 RESULTS AND DISCUSSION

3.1 | EBSD results

To avoid ambiguity, all crystallographic planes and directions in this study are denoted in terms of Miller–Bravais indices of a non-primitive hexagonal unit cell. Figure 1 demonstrates EBSD characterization of the as-grown, sectioned, and polished crystals. All inverse pole figure maps are plotted using the orientation of surface plane, with a step size of 1 μ m. Figure 1A shows a single crystal region

across a length scale of over 600 μm with no evidence of growth defects (e.g., twins, grain boundaries, secondary phases). The surface plane of this region is approximately $(\overline{2}\,1\,1\,16)$, 15° off the (0001) plane. Figure 1B shows another region that contains two families of growth twins in the same crystal. The EBSD maps shown in Figure 1C,D are representative regions in other sections of the crystal. Although growth twins were also observed, single crystal regions over 100 μm were routinely obtained and their surface planes (rounded to low indices) were determined as $(\overline{3}\,2\,1\,2)$, $(\overline{3}\,\overline{3}\,6\,4)$, and $(1\,4\,\overline{5}\,7)$; with the latter being 14° off the $(0\,1\,\overline{1}\,1)$ plane.

In addition to assessing the growth quality, the observed trace lines of the twin boundaries were used to estimate in-plane directions of the crystals. For instance, the two variants of crystals in Figure 1C were found to be divided by a twin boundary that resides in the $(0\,\bar{1}\,1\,1)$ plane in the $(\bar{3}\,2\,1\,2)$ oriented crystal (light green). Alternatively, the twin boundary inhabits the $(\bar{1}\,1\,0\,1)$ plane in the $(\bar{3}\,\bar{3}\,6\,4)$ oriented crystal (light cyan). Thus, in-plane direction of the trace line (rounded to low indices) was determined as $[2\,1\,\bar{3}\,4]$ and $[\bar{3}\,1\,2\,\bar{4}]$ on the $(\bar{3}\,2\,1\,2)$ and $(\bar{3}\,\bar{3}\,6\,4)$ oriented crystals, respectively. These were taken as the reference directions for the study of in-plane anisotropic nanoindentation behavior of the single crystals.

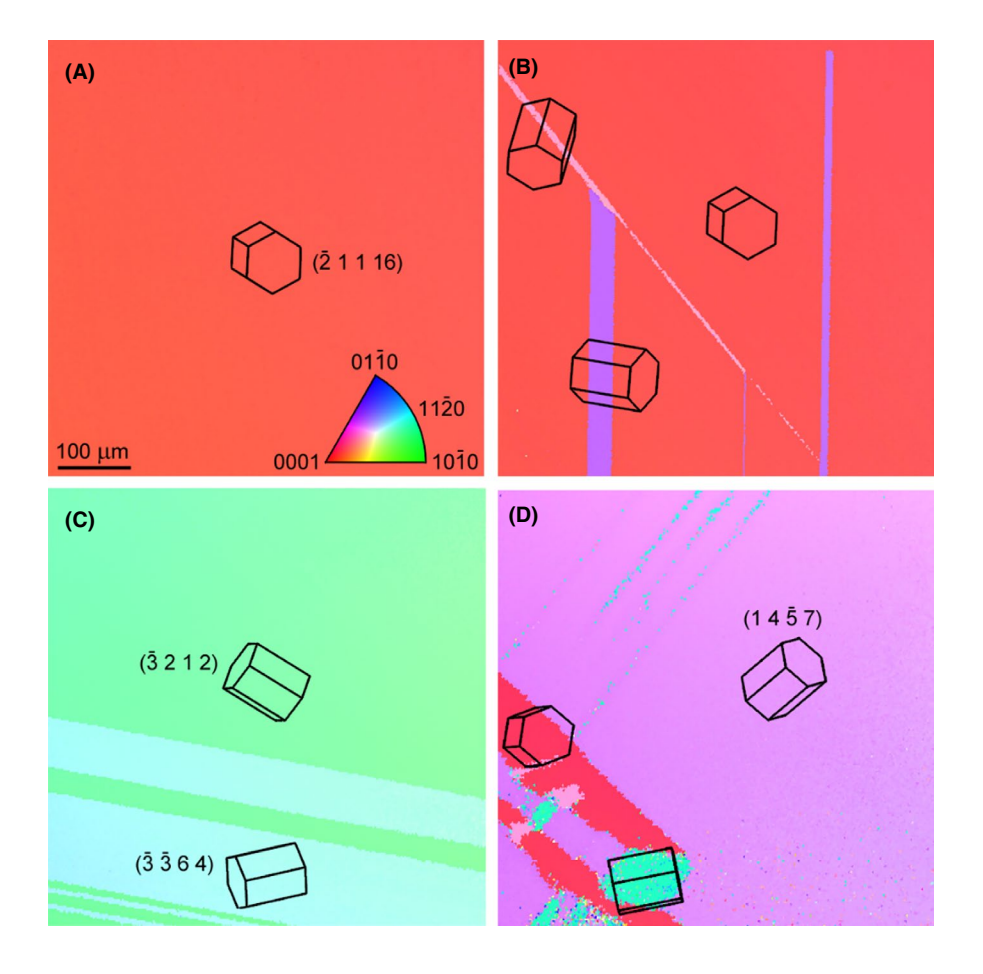
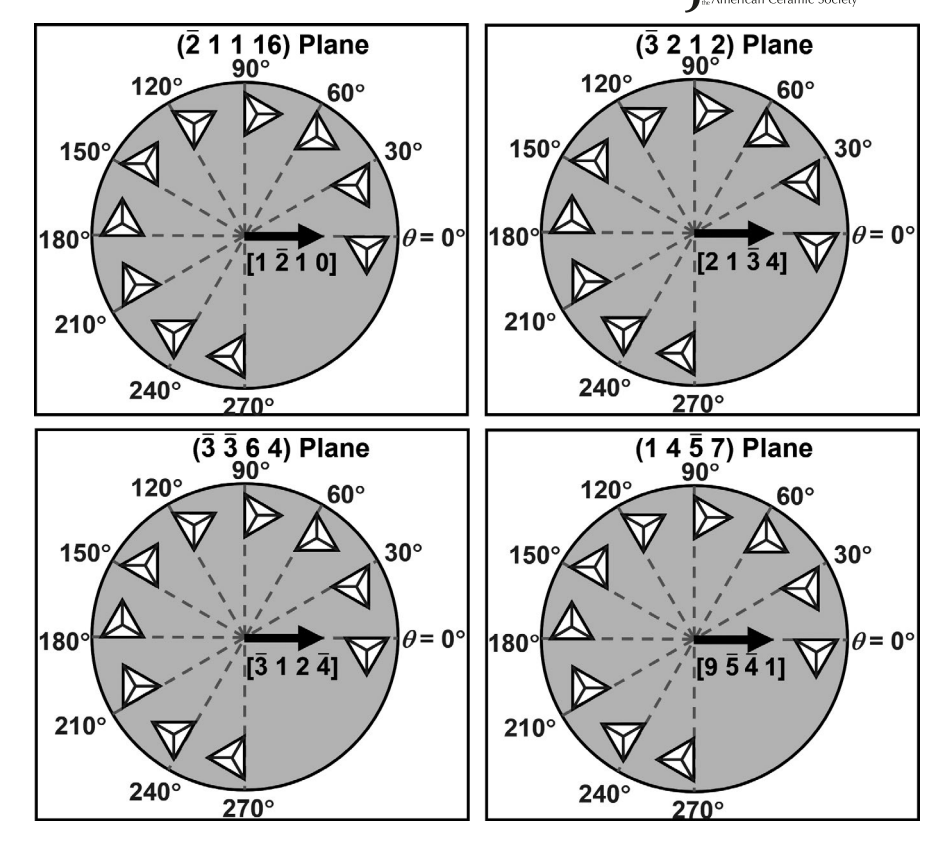


FIGURE 1 Representative EBSD orientation maps of (A and B) $(\overline{2}1116)$, (C) $(\overline{3}212)$, $(\overline{3}\overline{3}64)$, and (D) $(14\overline{5}7)$ surface planes in the as-grown crystals. Inset hexagonal prisms represent local top view of the crystal lattice

FIGURE 2 Schematic representation of the array of Berkovich indentations. For each single crystal region, orientations of the surface plane and reference in-plane direction are noted



3.2 Nanoindentation results

Figure 2 shows a schematic representation of the indentation array performed on each single crystal region. To study in-plane variations of indentation modulus and hardness, the angle (θ) between one facet edge of the Berkovich indenter and the reference direction (identified through EBSD characterization) was monitored. Indentations were repeated for θ values of 0–270° at increments of 30°. Indentation modulus and hardness were obtained using the traditional relationships described in Equations (2) and (3)—note that these relationships assume that the target material is isotropic.

Figure 3 shows the values of indentation modulus and hardness obtained at different θ values for the single crystal regions. Each data point is the average of at least five indentations over the depth range of 150-300 nm and the error bars represent plus/minus one standard deviation. We see that the indentation modulus and hardness vary by a significant margin with the indenter rotation angle for each of the planes that were indented. Given the threefold symmetry of the Berkovich indenter, one expects to obtain indistinguishable values of indentation modulus and hardness once the indenter is rotated by 120°. However, the indentation results reported in Figure 3 for nominally equivalent rotation angles are not always comparable (see, e.g., the values obtained at $\theta = 30$, 150, and 270° in Figure 3C,D). To investigate further, spatial maps of indentation modulus and hardness were obtained by

performing additional indentations at rotation angles of 30, 150, and 270° on the $(\overline{3}\,\overline{3}\,64)$ plane (details of these experiments are described in the supplementary Section S1 and Figure S1). Similar maps were also obtained at $\theta = 150$ and 270° on the $(14\overline{5}7)$ plane. Figure S2 shows the spatial maps of indentation modulus and the corresponding cumulative distributions and boxplots. For each map, the values of indentation modulus are seen to spread within a wide range. In some cases, the range of the spread is also seen to change significantly form one map to another (compare, e.g., the boxplots corresponding to the maps obtained at $\theta = 150$ and 270° on the $(14\overline{5}7)$ plane). Spatial variations in the stoichiometry of the single crystals¹³ is a plausible explanation for the observed scatter in the data. Even when this scatter is taken into account, the cumulative distributions and median values of indentation modulus at nominally equivalent rotation angles are statistically different. These observations are further supported by the spatial maps of indentation hardness and the corresponding cumulative distributions and boxplots shown in Figure S3. Visual inspection of the Berkovich tip with SEM showed noticeable differences in the topography of the three facets (see Figure S4). Such geometrical imperfections could contribute to the observed discrepancy²⁶ and thus complicate any inference about in-plane anisotropy of the single crystals.

We now turn our attention to out-of-plane variations in indentation modulus and hardness. Our indentation results in Figure 3 show a ~17% difference between the

highest (544 GPa obtained at $\theta = 240^{\circ}$ on the $(\overline{3}\,\overline{3}\,64)$ plane) and lowest (465 GPa obtained at $\theta = 270^{\circ}$ on the $(14\overline{5}7)$ plane) values of indentation modulus, demonstrating a strong overall out-of-plane anisotropy in the elasticity of the crystals. This is further supported by comparing the values of indentation modulus from the spatial maps obtained at a given rotation angle on the $(\overline{3}\,\overline{3}\,6\,4)$ and $(14\overline{5}7)$ planes (Figure S2). We note that indentations onto the (0001) plane were made by Domnich et al., 10 who observed an indentation modulus of 532 GPa while Straker et al. 11 estimated a modulus of 520 GPa. Domnich et al. 10 also measured a modulus of 548 GPa on the $(10\overline{1}1)$ plane, indicating some anisotropy as well. Previous studies on nanoindentation of materials with a large modulus-tohardness ratio demonstrated that application of the CSM technique could lead to a significant underestimation of indentation modulus (depending on the choice of harmonic oscillation parameters). 27 However, the higher end

of our indentation modulus values are comparable with the results obtained from nanoindentation experiments without the superimposed CSM oscillations.¹⁰

In terms of hardness, the nanoindentation results presented in Figure 3 and Figure S3 suggest the overall degree of out-of-plane variations in indentation hardness to be smaller than those in modulus. Nevertheless, the differences are still measurable within the uncertainty of our measurements. The range of our obtained hardness values (45–51 GPa) is higher than the previous reports on B_4C , $B_{4.9}C$, and $B_{4.9}C$ single crystals that reported values within a range of 41–45 GPa. 10,11,20,28 Further work to determine the cause of this discrepancy is warranted.

For different orientations of single crystals, Figure 4 shows the representative indentation depth profiles of hardness and the corresponding load vs. depth curves obtained at $\theta = 0^{\circ}$. The hardness depth profile of the $(\overline{2}\,1\,1\,16)$ plane is mostly smooth, and no serrations are observed in

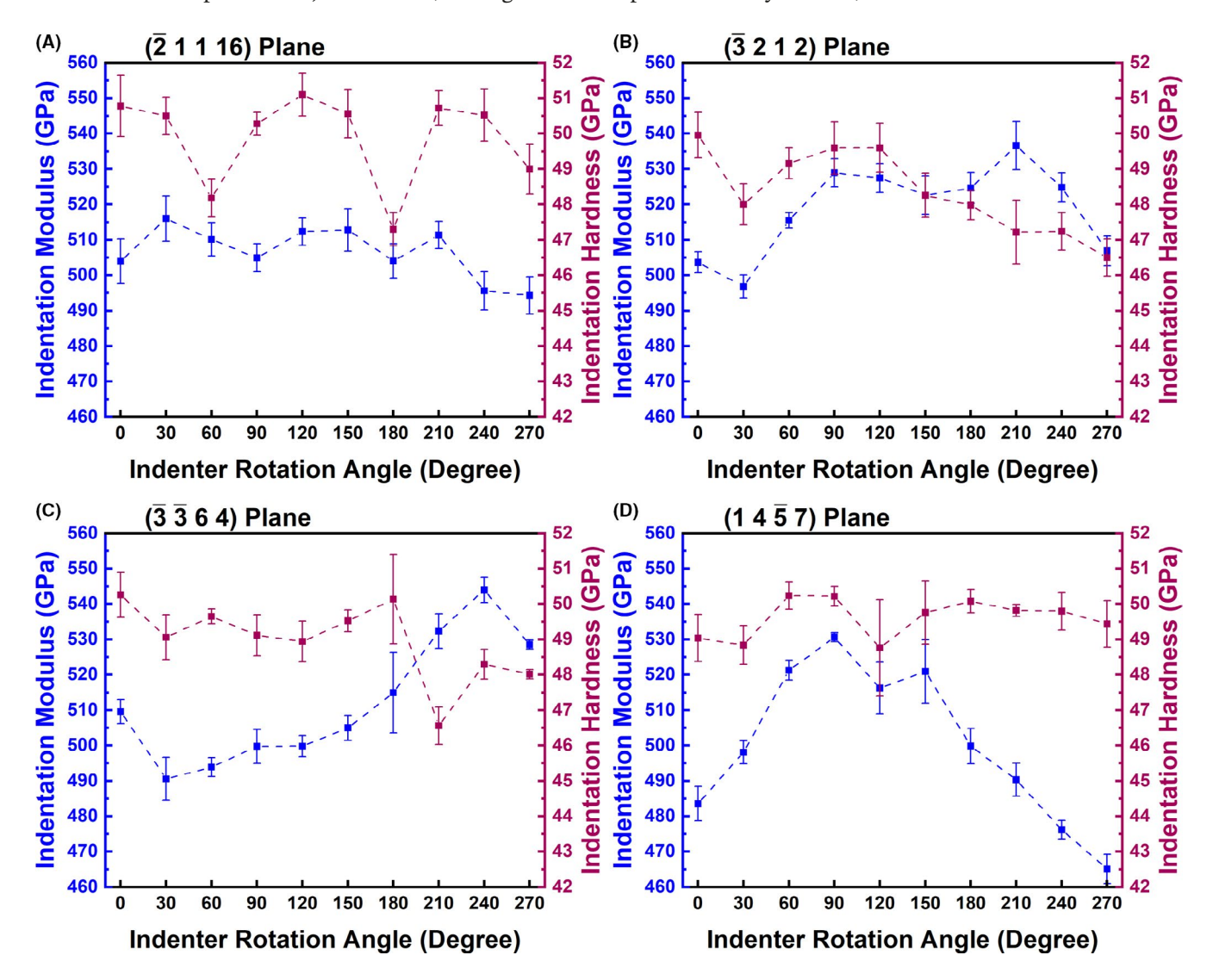


FIGURE 3 The orientation dependence of indentation modulus and hardness for (A) $(\overline{2}1116)$, (B) $(\overline{3}212)$, (C) $(\overline{3}\overline{3}64)$, and (D) $(14\overline{5}7)$ boron carbide single crystals

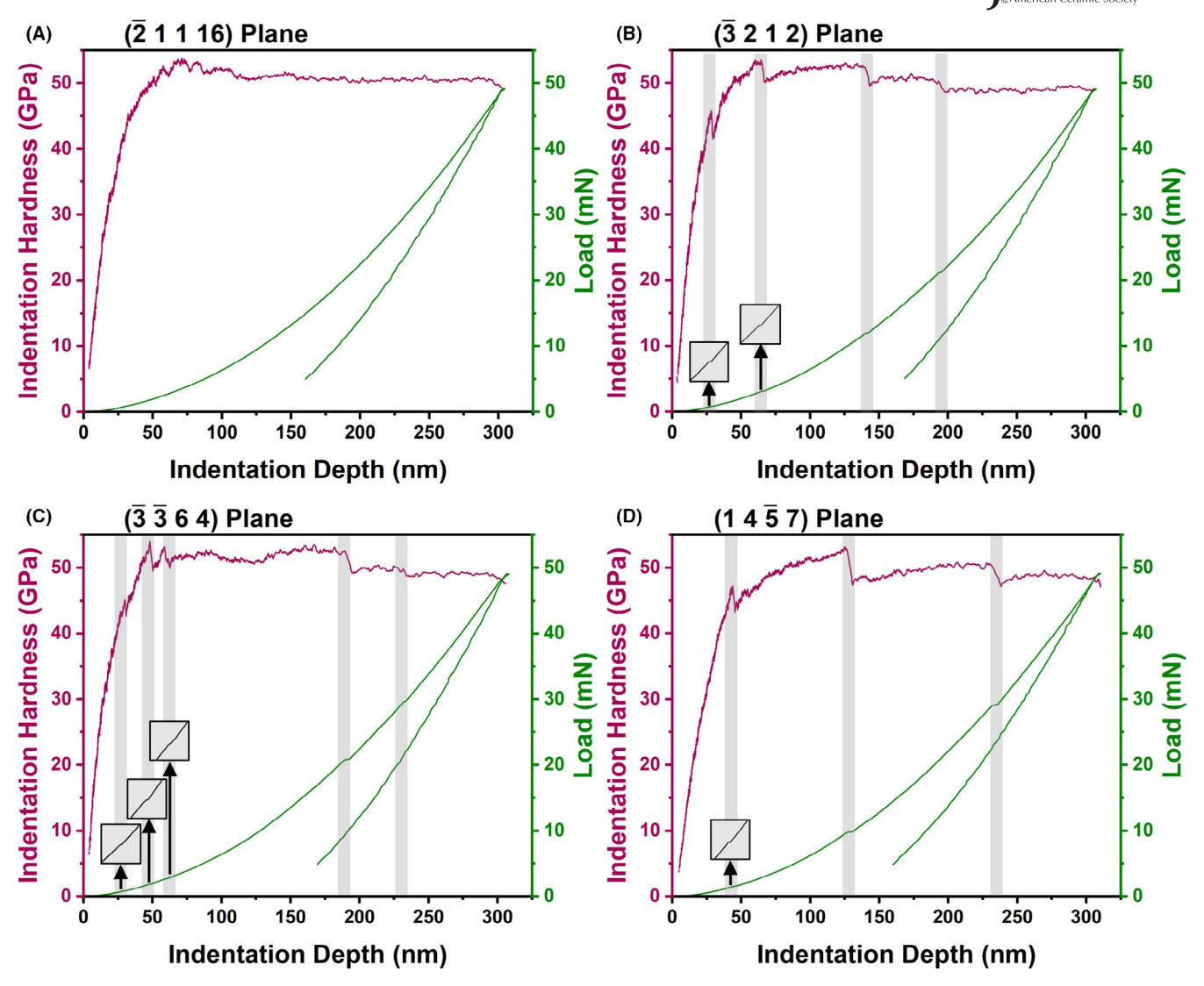


FIGURE 4 Representative depth profiles of indentation hardness and the corresponding load vs. depth curves obtained at $\theta = 0^{\circ}$ for (A) $(\overline{2}1116)$, (B) $(\overline{3}212)$, (C) $(\overline{3}\overline{3}64)$, and (D) $(14\overline{5}7)$ boron carbide single crystals. Each shaded region shows an abrupt drop in measured hardness and a corresponding pop-in event. Insets show a closer look of the pop-ins

the loading portion of the corresponding load vs. depth curve. In contrast, for all other orientations of the single crystals, increasing the indentation depth is seen to result in abrupt drops in the measured hardness values (highlighted in the shaded regions). A close examination of the corresponding load vs. depth curves revealed that each drop in hardness is associated with a sudden burst in indentation depth at a relatively constant load. These displacement bursts, commonly referred to as pop-ins, have been observed during nanoindentation of a variety of materials including ceramics, metals, semiconductors, and amorphous materials. Such pop-ins are generally attributed to various mechanisms of quasi-plastic/plastic instabilities such as phase transformation, ²⁹ deformation via slip/defect propagation, 29,30 discontinuous crack extension/chipping,³¹ and formation of shear³² or amorphous²⁸ bands. Although the exact nature of the corresponding

instability mechanisms in our study is uncertain, our observations suggest that activation of these mechanisms occurs during loading and results in a reduction in the measured indentation hardness.

To further examine the pop-in phenomenon, 12 indentations were performed at $\theta=0^\circ$ on each single crystal without the superimposed CSM oscillations. The obtained force vs. penetration depth curves (shown in Figure S5) were used to identify the load at which the first pop-in occurred. The results are summarized in Figure 5, where open symbols are used to distinguish the indentations that did not show a discernable pop-in. Consistent with the observation from the depth profiles of indentation hardness, pop-ins were less frequently observed on the $(\overline{2}\,1\,1\,16)$ plane. Considering that microstructural analysis of the indented regions on this plane (discussed in detail in Section 3.3) showed evidence of quasi-plasticity, the less frequent observation of indentation

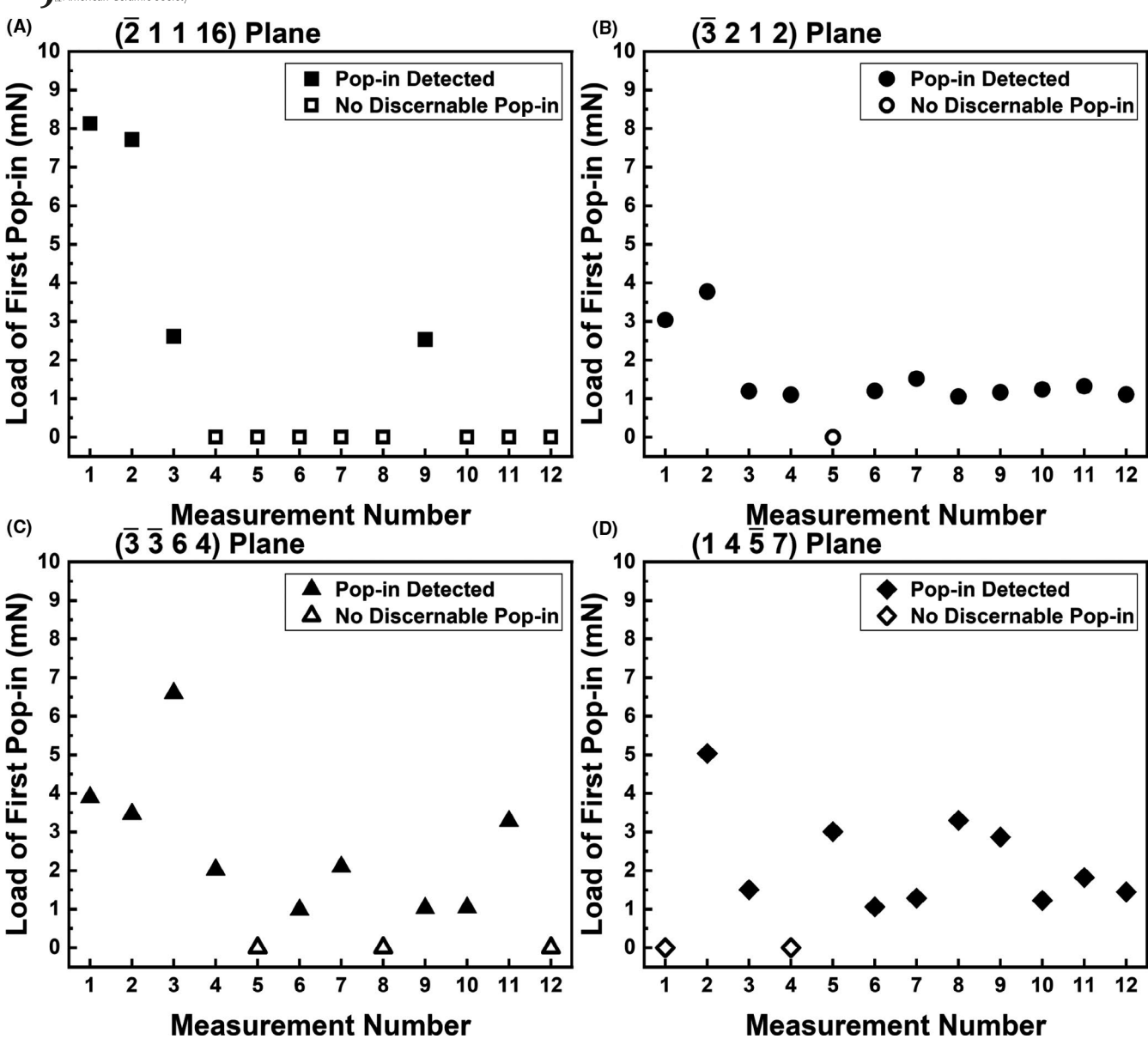


FIGURE 5 Values of load corresponding to the first pop-in from the indentations performed without the CSM oscillations at $\theta = 0^{\circ}$ on the (A) $(\overline{2}1116)$, (B) $(\overline{3}212)$, (C) $(\overline{3}\overline{3}64)$, and (D) $(14\overline{5}7)$ boron carbide single crystals

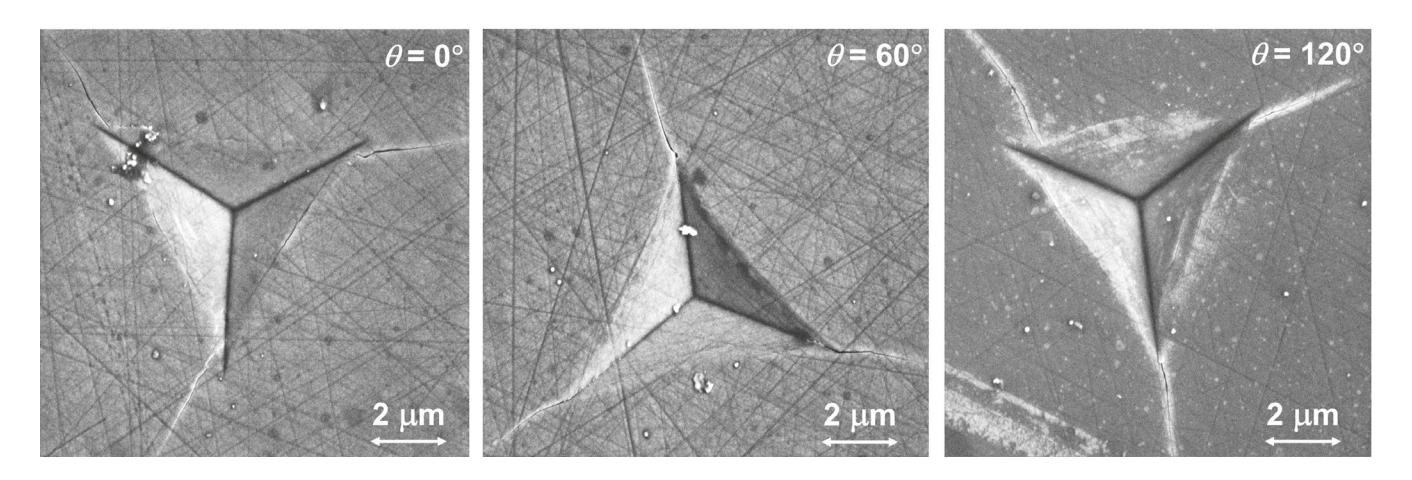


FIGURE 6 Post-indentation SEM images of Berkovich indentations on the $(\bar{2}1116)$ plane to a maximum indentation depth of ~1 μ m

pop-ins seems to suggest that the quasi-plastic flow along this orientation of the single crystals is more homogeneous. Similar observations have been reported for B₄C single crystals oriented along the $(1\overline{4}35)$ plane where the absence of indentation pop-ins was attributed to simultaneous activation of multiple shear bands during deformation.²⁸ In contrast to the $(\overline{2} \, 1 \, 1 \, 16)$ plane, pop-ins were frequently observed for other orientations of the single crystals, and the load at which the first pop-in occurred was found to be highly repeatable on the (3 2 1 2) plane. When indentations were performed on this plane using a maximum load smaller than the load of first pop-in (see the inset of Figure S5b), the unloading curve was found to fully retrace the loading curve, suggesting that deformation is entirely elastic prior to the first pop-in. This is consistent with the previous reports on nanoindentation of defect-free single crystals that attributed the first pop-in to the onset of plasticity.^{28,33–37}

Figure S6 shows the representative SEM images of the residual impressions obtained from Berkovich indentations with a maximum indentation depth of ~300 nm on different single crystal regions. No evidence of pile-up is observed around the edges of the impressions, confirming that the projected contact area determined by the Oliver and Pharr method²⁵ is not underestimated. Even though the SEM images do not rule out occurrence of sink-in, we note that the ratio of final indentation depth to maximum indentation depth ($h_{\rm f}/h_{\rm max}$) for our single crystals is within a range of 0.43–0.50. It has been shown that when $h_{\rm f}/h_{\rm max} < 0.7$, the Oliver and Pharr²⁵ contact area matches very well with true contact area even if sink-in is present.³⁸

Although surface cracks were observed in some cases, a clear visualization of these proved to be challenging due to their relatively small length (\leq 500 nm). Representative SEM images of the indentations performed to a maximum depth of 1 μ m on the ($\overline{2}$ 1 116) plane are shown in Figure 6. Radial cracks, nearly 2.5–3.0 μ m long, were consistently observed at $\theta=0$, 60, and 120°. The radial cracks were always found to be emanating from the corners of the impressions made at $\theta=60^\circ$, but the same was not true for $\theta=0$ and 120°. Nevertheless, for each θ value, the surface directions along which the cracks propagated were found to be highly repeatable, suggesting that preferred surface directions exist for propagation of indentation cracks.

3.3 | Post-indentation TEM results

Cross-sectional specimens were extracted under the indentations performed on different single crystal regions. The microscopic deformation mechanisms that are demonstrated herein are ubiquitous in all examined specimens, with shallow (~300 nm) and deep (~1 μ m) indents in the ($\overline{2}1116$) oriented crystal taken as examples. The

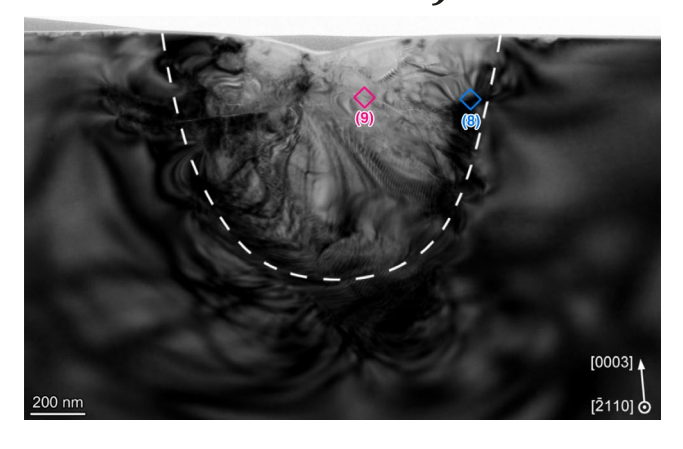


FIGURE 7 TEM bright field image of cross-sectional specimen under a shallow indent in the $(\overline{2}1116)$ plane. Dashed curve indicates the quasi-plastic region

corresponding θ values for these indentations were 0 and 60° (see Figure 2). Figure 7 shows a TEM bright field image of the deformation zone under a shallow indent. With the un-deformed region tilted into a $\left[2\,1\,1\,0\right]$ zone axis, the brighter diffraction contrast beneath the indent (marked with dash curve) indicates the region with remarkable quasi-plastic strain, that is, in the form of lattice rotation and various microstructural defects. A depth of ~800 nm was estimated for the quasi-plastic region in this specimen.

Detailed imaging and diffraction analyses³⁹ revealed a large number of planar defects, shown as narrow bands, in the quasi-plastic region. Moreover, high-resolution (HR) TEM images show good alignment between these bands of localized deformation with a variety of low-index crystallographic planes. For instance, Figure 8A shows an HRTEM image of a crystal slip in the (0003) plane and the shear displacement associated with this defect is clearly seen in the Fourier-filtered image that is shown in Figure 8B. The slip plane is atomically sharp when viewed edge-on, with no discernible evidence of amorphization (as described below). Defects of this type were frequently observed at the periphery of the quasiplastic region (e.g., blue square (8) in Figure 7) that was subjected to a lower level of stress. Thus, it appears that the initial stage of quasi-plastic deformation is mediated by such atomic scale shearing/slip activities. These observations are in good agreement with previous HRTEM characterization at the tip of amorphous bands.⁴⁰

Figure 9 shows an HRTEM image from the center of the quasi-plastic region (e.g., red square (9) in Figure 7). For a conical indenter tip with the same centerline-to-face angle as Berkovich, increasing the lateral distance from the indenter apex at a given indentation depth results in a reduction in the theoretical values of principal normal, maximum shear, and hydrostatic stress components.⁴¹ Therefore, we hypothesize the stress in

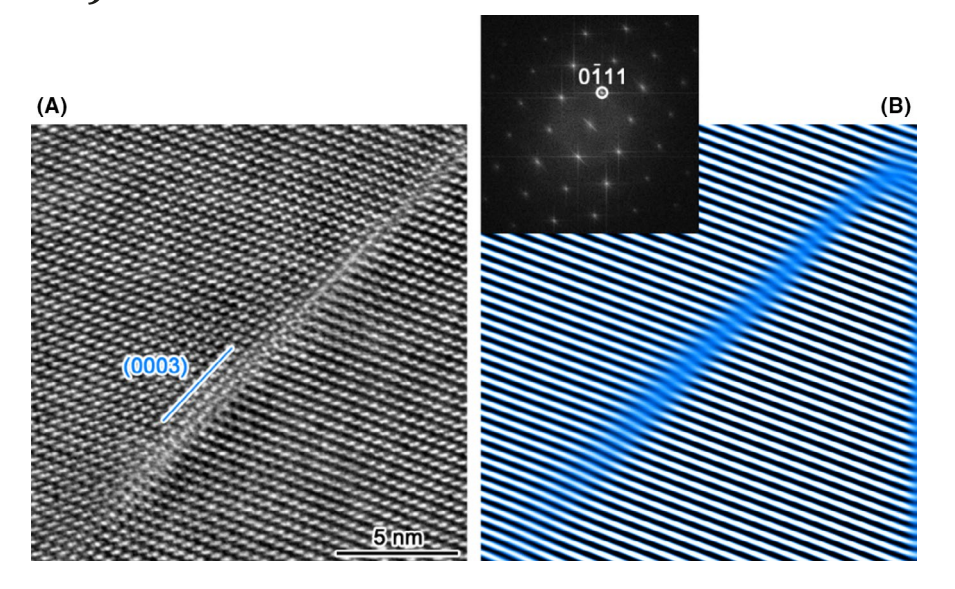
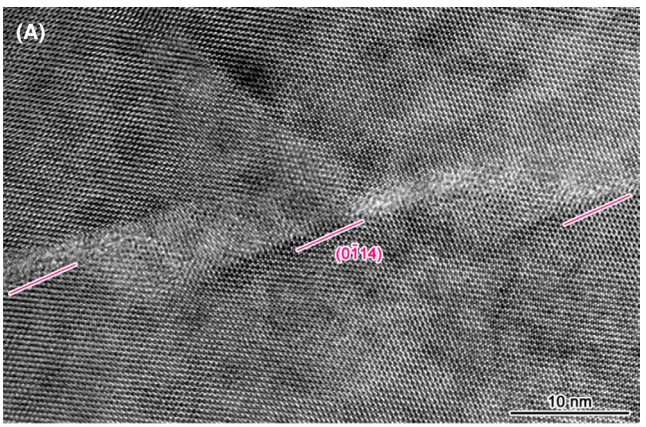


FIGURE 8 Representative planar defect at the periphery of quasi-plastic region (square area (8) in Figure 7). (A) HRTEM image of an atomic slip plane in the $(0\,0\,0\,3)$ plane as viewed edge-on. (B) Inverse Fourier Transform image of (A) made using the $[0\,\overline{1}\,1\,1]$ reflection highlights the shear displacement. Inset shows the Fourier Transform pattern



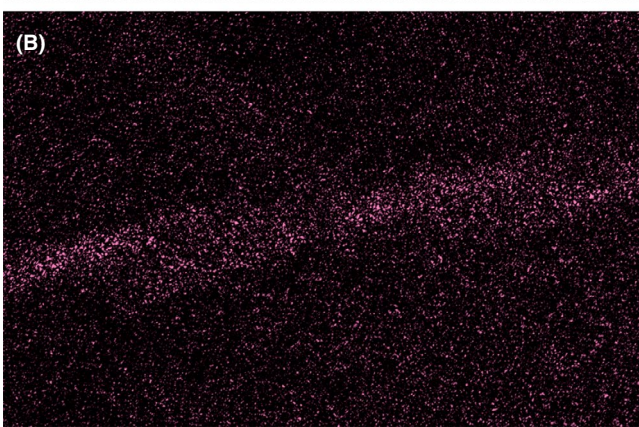


FIGURE 9 Representative planar defect at the center of quasi-plastic region (square area (9) in Figure 7). (A) HRTEM image of an amorphous band showing a "kinked" configuration with the segments in parallel $(0\bar{1}14)$ planes viewed edge-on. (B) Fourier filtered image of (A) highlighting the contrast of noncrystallinity in the amorphous band

the region marked by the red square (9) in Figure 7 to be more intense and more hydrostatic than the region marked in blue square (8). Further investigations to verify

this hypothesis for indentations with a Berkovich tip on boron carbide single crystals are warranted. To uncover greater details of defect morphology and the underlying propagation behavior, the raw HRTEM image (Figure 9A) was Fourier filtered to remove the contributions from all reflections in the crystal diffraction pattern; the filtered Inverse Fourier Transform image thereby highlights the high-frequency contrast variation, which was associated with non-crystallinity due to formation of lattice defects and/or an amorphous phase. By this means, Figure 9B reveals an amorphous band with an intriguing three-dimensionally kinked morphology: some segments are narrower (~2 nm) and are well aligned with a parallel set of edge-on $(0\overline{1}14)$ planes, whereas the intermediate segments appear to be wider, indicating other habit planes. The mechanism (e.g., the role of crystal anisotropy, local stress field, and chemistry) that impeded the straight propagation of amorphous bands remains to be clarified. Nonetheless, our observations³⁹ provide direct evidence that amorphous bands prefer to form along specific low-index planes, but are also likely to toggle between different planes, leading to three-dimensional propagation at the nanoscale. It is further hypothesized that the adaptability of amorphous bands to varied crystallographic planes may explain previous observations that some amorphous bands appeared to align, but inaccurately, with low-index planes. 3,5,42,43

Figure 10 shows a TEM bright field image of the deformed crystal under a ~1 μm indent, with the undeformed region tilted into a $\left[1\,\overline{2}\,1\,0\right]$ zone axis. Similar to Figure 7, the brighter diffraction contrast beneath the indent (outlined with a white dashed line) indicates the quasi-plastic region, with a much greater depth of ~3 μm . Both observations point to a range of quasi-plasticity that is ~3 times the maximum indentation depth. Cracks were found to extend far beyond the quasi-plastic region, as has

FIGURE 10 TEM bright field image of cross-sectional specimen under a deep indent in $(\overline{2}1116)$ plane. Dashed curve indicates the quasi-plastic region

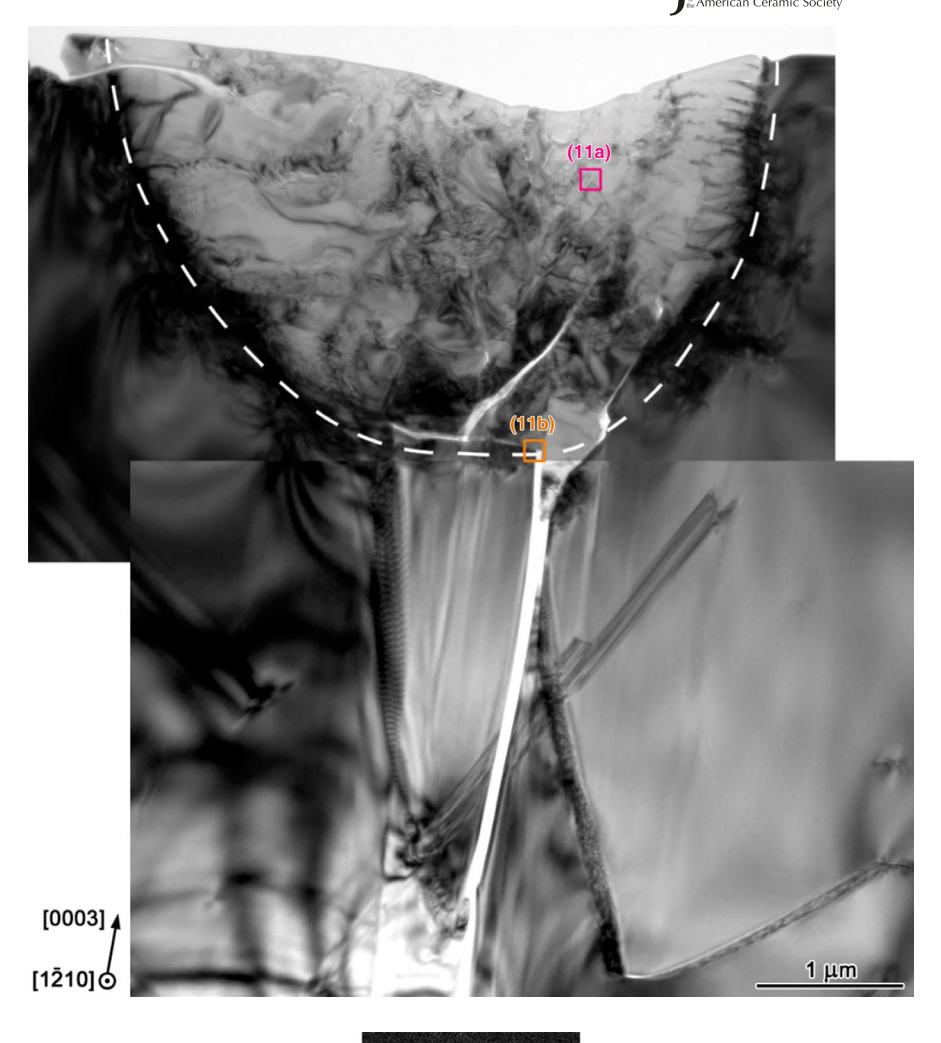
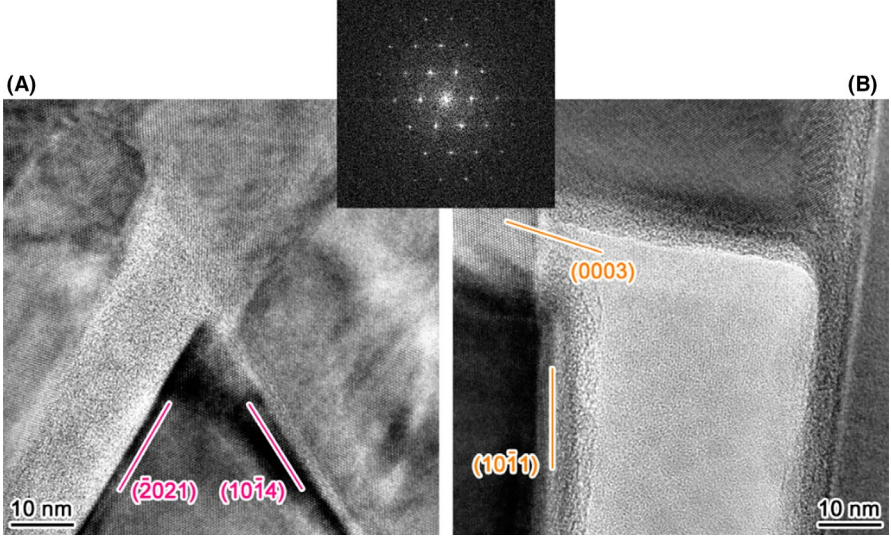


FIGURE 11 Defect evolution and failure under the deep indent. (A) HRTEM image of the square area (11a) in Figure 10 shows amorphous bands in varied planes. (B) HRTEM image of the square area (11b) in Figure 10 shows crystal fragmentation along varied planes. Inset shows the Fourier Transform pattern



also been observed in previous characterization under Vickers indentations. 44

Figure 11 demonstrates the connection between amorphous band formation and the later stage of deformation and material failure. Figure 11A shows a representative HRTEM image in the quasi-plastic region (at square area (11a) in Figure 10), wherein the amorphous bands were

substantially developed in thickness (~15 nm) and formed along multiple low-index planes. The variation of contrast indicates that the original single crystal was divided by the amorphous bands into nanosized pieces with remarkable misorientation in between. Going deeper under the indent, where the cracks extend beyond the range of quasiplasticity, they are always found to initiate from within the

quasi-plastic region and are also aligned with low-index planes (as shown in Figure 11B, taken at square area (11b) in Figure 10). This suggests that the development of localized amorphization leads to fracture and fragmentation of crystal, as also proposed in our original report of the phenomenon.³ We also note that not all the observed amorphous bands evolve into cracks, suggesting that the crystal anisotropy and the character of the local stress field may also be relevant to the evolution from amorphous bands to intragranular cracks.

4 | SUMMARY AND CONCLUSIONS

Boron carbide single crystals were prepared by optical floating zone method and their mechanical response was investigated by nanoindentation experiments using a Berkovich indenter tip. Results showed indentation modulus and hardness could vary significantly by changing out-of-plane crystallographic orientation. Variations of modulus and hardness with indenter rotation in the plane of the indentation were also observed but found to be influenced by the scatter in the data and geometrical imperfections of the indenter tip. Through the use of the CSM technique, it was shown that abrupt activation of quasi-plasticity mechanisms results in manifestation of pop-ins in the load vs. depth curves. Pop-ins were found to be suppressed when indentations were performed along the (21116) orientation of the single crystals suggesting simultaneous activation of quasi-plasticity mechanisms during deformation. Post-indentation TEM micrographs and diffraction analysis of the quasi-plastic region under Berkovich indents uncovered crystal slip planes and evidenced amorphous bands that were formed in multiple crystallographic planes in 3D. Based on the initiation and propagation of stress-induced amorphization, the mechanism of quasi-plasticity and failure was clarified as follows: atomic slip, amorphous band formation, and fracture.

ACKNOWLEDGMENTS

Research was sponsored by the Army Research Laboratory and was accomplished under Cooperative Agreement Number W911NF-12-2-0022. The views and conclusions contained in this document are those of the authors and should not be interpreted as representing the official policies, either expressed or implied, of the Army Research Laboratory or the U.S. Government. The U.S. Government is authorized to reproduce and distribute reprints for Government purposes notwithstanding any copyright notation herein.

ORCID

REFERENCES

- Domnich V, Reynaud S, Haber RA, Chhowalla M. Boron carbide: Structure, properties, and stability under stress. J Am Ceram Soc. 2011;94(11):3605–28. https://doi.org/10.1111/ j.1551-2916.2011.04865.x
- Awasthi A, Subhash G. Deformation behavior and amorphization in icosahedral boron-rich ceramics. Prog Mater Sci. 2020;112:100664. https://doi.org/10.1016/j.pmatsci.2020. 100664
- Chen MW, McCauley JW, Hemker KJ. Shock-induced localized amorphization in boron carbide. Science. 2003;299(5612):1563– 6. https://doi.org/10.1126/science.1080819
- Fanchini G, McCauley JW, Chhowalla M. Behavior of disordered boron carbide under stress. Phys Rev Lett. 2006;97:035502. https://doi.org/10.1103/PhysRevLett.97.035502
- Yan XQ, Tang Z, Zhang L, Guo JJ, Jin CQ, Zhang Y, et al. Depressurization amorphization of single-crystal boron carbide. Phys Rev Lett. 2009;102:075505. https://doi.org/10.1103/ PhysRevLett.102.075505
- 6. An Q, Goddard WA. Atomistic origin of brittle failure of boron carbide from large-scale reactive dynamics simulations: Suggestions toward improved ductility. Phys Rev Lett. 2015;115:105501. https://doi.org/10.1103/PhysRevLett.115.105501
- Korotaev P, Pokatashkin P, Yanilkin A. The role of nonhydrostatic stresses in phase transitions in boron carbide. Comput Mater Sci. 2016;121:106–12. https://doi.org/10.1016/j. commatsci.2016.04.041
- Awasthi AP, Subhash G. High-pressure deformation and amorphization in boron carbide. J Appl Phys. 2019;125(21):215901. https://doi.org/10.1063/1.5091795
- An Q, Goddard WA, Cheng T. Atomistic explanation of shearinduced amorphous band formation in boron carbide. Phys Rev Lett. 2014;113:095501. https://doi.org/10.1103/PhysR evLett.113.095501
- Domnich V, Gogotsi Y, Trenary M, Tanaka T. Nanoindentation and Raman spectroscopy studies of boron carbide single crystals. Appl Phys Lett. 2002;81(20):3783. https://doi. org/10.1063/1.1521580
- Straker M, Chauhan A, Sinha M, Phelan WA, Chandrashekhar MVS, Hemker KJ, et al. Growth of high purity zone-refined boron carbide single crystals by laser diode floating zone method. J Cryst Growth. 2020;543(1):125700. https://doi. org/10.1016/j.jcrysgro.2020.125700
- 12. McClellan KJ, Chu F, Roper JM, Shindo I. Room temperature single crystal elastic constants of boron carbide. J Mater Sci. 2001;36:3403–7. https://doi.org/10.1023/A:1017947625784
- 13. Taylor DE, McCauley JW, Wright TW. The effects of stoichiometry on the mechanical properties of icosahedral boron carbide under loading. J Phys Condens Matter. 2012;24:505402.
- Clayton JD. Towards a nonlinear elastic representation of finite compression and instability of boron carbide ceramic. Philos Mag. 2012;92(23):2860–93. https://doi.org/10.1080/14786 435.2012.682171
- Dresch AB, Venturini J, Arcaro S, Montedo ORK, Bergmann CP.
 Ballistic ceramics and analysis of their mechanical properties for armour applications: A review. Ceram Int. 2021;47(7):8743– 61. https://doi.org/10.1016/j.ceramint.2020.12.095
- Hallam D, Heaton A, James B, Smith P, Yeomans J. The correlation of indentation behaviour with ballistic performance for spark plasma

- sintered armour ceramics. J Eur Ceram Soc. 2015;35(8):2243–52. https://doi.org/10.1016/j.jeurceramsoc.2014.11.035
- Haney EJ, Subhash G. Damage mechanisms perspective on superior ballistic performance of spinel over sapphire. Exp Mech. 2013:53:31–46. https://doi.org/10.1007/s11340-012-9634-0
- McCauley JW, Wilantewicz TE. Using plasticity values determined from systematic hardness indentation measurements for predicting impact behavior in structural ceramics: A new, simple screening technique. Proceedings of the 26th Army Science Conference. 2009.
- Gunjushima I, Akashi T, Goto T. Thermoplastic properties of single crystalline B₄C prepared by a floating zone method. Mater Trans. 2001;42(7):1445–50. https://doi.org/10.2320/matertrans.42.1445
- Yan XQ, Li WJ, Goto T, Chen MW. Raman spectroscopy of pressure-induced amorphous boron carbide. Appl Phys Lett. 2006;88(13):131905. https://doi.org/10.1063/1.2189826
- 21. Chudoba T, Schwaller P, Rabe R, Breguet J-M, Michler J. Comparison of nanoindentation results obtained with Berkovich and cube-corner indenters. Philos Mag. 2006;86(33-35):5265–83. https://doi.org/10.1080/14786430600746424
- Pethica JB, Oliver WC. Mechanical properties of nanometre volumes of material: Use of the elastic response of small area indentations. MRS Online Proceedings Library. 1988;130:13– 23. https://doi.org/10.1557/PROC-130-13
- 23. Oliver WC, Pharr GM. Measurement of hardness and elastic modulus by instrumented indentation: Advances in understanding and refinements to methodology. J Mater Res. 2004;19(1):3–20. https://doi.org/10.1557/jmr.2004.19.1.3
- 24. Hay J, Agee P, Herbert E. Continuous stiffness measurement during instrumented indentation testing. Exp Tech. 2010;34:86–94. https://doi.org/10.1111/j.1747-1567.2010.00618.x
- 25. Oliver WC, Pharr GM. An improved technique for determining hardness and elastic modulus using load and displacement sensing indentation experiments. J Mater Res. 1992;7(6):1564–83. https://doi.org/10.1557/JMR.1992.1564
- 26. Chen S, Miyahara Y, Nomoto A. Crystallographic orientation dependence of nanoindentation hardness in austenitic phase of stainless steel. Philos Mag Lett. 2018;98(11):473–85. https://doi.org/10.1080/09500839.2019.1577997
- Merle B, Maier-kiener V, Pharr GM. Influence of modulusto-hardness ratio and harmonic parameters on continuous stiffness measurement during nanoindentation. Acta Mater. 2017;134(1):167–76. https://doi.org/10.1016/j.actamat.2017.05.036
- Reddy KM, Guo D, Song S, Cheng C, Han J, Wang X, et al. Dislocation-mediated shear amorphization in boron carbide. Sci Adv. 2021;7:eabc6714. https://doi.org/10.1126/sciadv.abc6714
- 29. Huston LQ, Kiran MSRN, Smillie LA, Williams JS, Bradby JE. Cold nanoindentation of germanium. Appl Phys Lett. 2017;111(2):021901. https://doi.org/10.1063/1.4993163
- Bradby JE, Williams JS, Wong-Leung J, Swain MV, Munroe P. Nanoindentation-induced deformation of Ge. Appl Phys Lett. 2002;80(15):2651. https://doi.org/10.1063/1.1469660
- 31. JangJ,LanceMJ,WenS,PharrGM.Evidencefornanoindentationinduced phase transformations in germanium. Appl Phys Lett. 2005;86:131907. https://doi.org/10.1063/1.1894588
- Lucca DA, Zare A, Klopfstein MJ, Shao L, Xie GQ. Investigation
 of the mechanical behavior of ion irradiated Ni-free Ti-based

- metallic glass by nanoindentation. CIRP Ann. 2014;63(1):533–6. https://doi.org/10.1016/j.cirp.2014.03.045
- Li TL, Gao YF, Bei H, George EP. Indentation Schmid factor and orientation dependence of nanoindentation pop-in behavior of NiAl single crystals. J Mech Phys Solids. 2011;59(6):1147– 62. https://doi.org/10.1016/j.jmps.2011.04.003
- 34. Bei H, Gao YF, Shim S, George EP, Pharr GM. Strength differences arising from homogeneous versus heterogeneous dislocation nucleation. Phys Rev B. 2008;77:060103. https://doi.org/10.1103/PhysRevB.77.060103
- Lucca DA, Klopfstein MJ, Ghisleni R, Cantwell G. Investigation of polished single crystal ZnO by nanoindentation. CIRP Ann. 2002;51(1):483–6. https://doi.org/10.1016/S0007-8506(07)61566-2
- Datye A, Li L, Zhang W, Wei Y, Gao Y, Pharr GM. Extraction of anisotropic mechanical properties from nanoindentation of SiC-6H single crystals. J Appl Mech. 2016;83(9):091003. https:// doi.org/10.1115/1.4033790
- Page TF, Oliver WC, McHargue CJ. The deformation behavior of ceramic crystals subjected to very low load (nano)indentations. J Mater Res. 1992;7(2):450–73. https://doi.org/10.1557/ JMR.1992.0450
- Bolshakov A, Pharr GM. Influences of pileup on the measurement of mechanical properties by load and depth sensing indentation techniques. J Mater Res. 1998;13(4):1049–58. https://doi.org/10.1557/JMR.1998.0146
- 39. He M-R, Zare A, Mitra N, Li W, Straker M, Spencer M, et al. On the initiation and evolution of stress-induced amorphization in boron carbide single crystals. (Unpublished).
- Reddy KM, Liu P, Hirata A, Fujita T, Chen MW. Atomic structure of amorphous shear bands in boron carbide. Nat Commun. 2013;4:2483. https://doi.org/10.1038/ncomms3483
- 41. Fischer-Cripps AC. Introduction to contact mechanics, 2nd edn. USA: Springer; 2007.
- 42. Ge D, Domnich V, Juliano T, Stach EA, Gogotsi Y. Structural damage in boron carbide under contact loading. Acta Mater. 2004;52(13):3921–7. https://doi.org/10.1016/j.actamat.2004.05.007
- Zhao S, Kad B, Remington BA, LaSalvia JC, Wehrenberg CE, Behler KD, et al. Directional amorphization of boron carbide subjected to laser shock compression. Proc Natl Acad Sci. 2016;113(43):12088–93. https://doi.org/10.1073/pnas.1604613113
- Subhash G, Ghosh D, Blaber J, Zheng JQ, Halls V, Masters K. Characterization of the 3-D amorphized zone beneath a Vickers indentation in boron carbide using Raman spectroscopy. Acta Mater. 2013;61(10):3888–96. https://doi.org/10.1016/j.actamat.2013.03.028

SUPPORTING INFORMATION

Additional supporting information may be found online in the Supporting Information section.

How to cite this article: Zare A, He M-R, Straker M, Chandrashekhare MVS, Spencer M, Hemker KJ, et al. Mechanical characterization of boron carbide single crystals. J Am Ceram Soc. 2021;00:1–13. https://doi.org/10.1111/jace.18065